Atmospheric Pollution Research 5 (2014) 601-609

Atmospheric Pollution Research

www.atmospolres.com

The mass concentration and optical properties of black carbon aerosols over a semi–arid region in the northwest of China

Xianjie Cao, Jiening Liang, Pengfei Tian, Lei Zhang, Xiaojing Quan, Weiping Liu

Key Laboratory for Semi–Arid Climate Change of the Ministry of Education, College of Atmospheric Sciences, Lanzhou University, 222 Tianshui South Road, Lanzhou, 730000, China

ABSTRACT

Black Carbon (BC) is the predominant absorption component of atmospheric aerosols, and it is believed to be the second largest contributor to global warming. Calculating its radiative forcing requires observational data regarding its physical, chemical and optical properties, so observation is the foundation of this research. The Semi–Arid Climate and Environment Observatory of Lanzhou University aims to improve our understanding in this regard by capturing direct evidence of the impact of human activity on the semi–arid climate over the Loess Plateau of Northwestern China. In this paper, the period from November 2010 to February 2011, which is within the heating period, was selected in order to study the optical properties of BC, such as its depolarization ratio, extinction coefficient, optical depth, Ångström exponent and effective radius. The average BC concentration was 2 334±1 546 ng/m^3 during the observation. The diurnal evolution of BC concentration had two maximums, which appeared at 10:00 and 20:00 (local time), and two minimums, which appeared at 03:00 and 16:00. The average Aerosol Optical Depth (AOD) during the observation was 0.26±0.2, the aerosols existed mostly between the surface of the Earth and a height of 3 km, and the extinction coefficient decreased with height. The average of the depolarization ratio between the surface of the Earth and a height of 3 km, the Ångström exponent ($\alpha_{440/870\ nm}$) and the effective radius of black carbon aerosols were 0.24, 0.86±0.30 and 0.54±0.17 μm, respectively. The maximum distribution frequency of $\alpha_{440/870\ nm}$ was 27%, with a range of 1.0 to 1.2. The maximum distribution frequency of the effective radius was 28%, with a range of 0.4 μm to 0.5 μm.

Keywords: *Black carbon, depolarization, extinction, lidar*

Corresponding Author:
Xianjie Cao
☎ : *+86-13919262560*
🖷 : *+86-0931-8914278*
✉ : *caoxj@lzu.edu.cn*

Article History:
Received: 21 January 2014
Revised: 24 April 2014
Accepted: 25 April 2014

doi: 10.5094/APR.2014.069

1. Introduction

Global climate change caused by anthropogenic activities has attracted worldwide attention for scientific and socio–economic reasons, and one of the important elements of global climate change is particulate matter, such as atmospheric aerosols (Sasano, 1996). Aerosols have direct and indirect radiative effects that occur via the scattering and absorbing of solar radiation (McCormick and Ludwig, 1967; Charlson and Pilat, 1969; Atwater, 1970; Coakley et al., 1983) and effects on clouds' microphysical properties in the form of Cloud Condensation Nuclei (CCN), such as increasing the cloud albedo and suppressing precipitation (Twomey, 1977; Albrecht, 1989). The scattering and absorbing of solar radiation can affect the atmospheric temperature profile and cloud formation, leading to changes in the energy budget of the Earth and its atmospheric system; that is a semi–direct effect of aerosols (Grassl, 1975; Hansen et al., 1997; Ackerman et al., 2000; Koren et al., 2004).

Black Carbon (BC) is caused by anthropogenic activities. It is produced via the incomplete combustion of fossil fuels, biofuels and biomass (Schwarz et al., 2006). Thirty–eight percent of global BC emissions is from fossil fuels, 20% is from biofuels and 42% is from the burning of biomass (Bond et al., 2004). BC absorbs both incoming and outgoing radiation, which contributes to the warming of the atmosphere and the cooling at the Earth's surface. BC also has a semi–direct effect by changing the surface albedo when it is deposited on snow and ice. Currently, BC is considered to be the second largest contributor to global warming, carbon dioxide being the largest (Ramanathan and Carmichael, 2008).

There is much research on the estimation of BC's radiative forcing. For example, the average atmospheric radiative forcing was +10±3 W/m^2 at Manora Peak, in the Indian Himalayan foothills (Srivastava et al., 2012); +71 W/m^2 in Kanpur, India (Tripathi et al., 2005); +28 W/m^2 in Bangalore, India (Babu et al., 2002), and +15~+30 W/m^2 over the coastal Arabian Sea (Babu et al., 2004). The simulation of the BC's radiative forcing depends on accurate and comprehensive observational data regarding its physical, chemical and optical properties [i.e., its Aerosol Optical Depth (AOD), single scatter albedo, asymmetry factor, chemical composition and size distribution] (Shi et al., 2008). Thus, observation is fundamental to research on radiative forcing's effect on climate change.

In this study, the observation was carried out at the Semi–Arid Climate and Environment Observatory of Lanzhou University (SACOL) from November 2010 to February 2011, which was within the heating period. It is reasonable to believe that BC was the predominant aerosols during the heating period. In this paper, the vertical distribution of the BC depolarization ratio and extinction coefficient, as well as the variation of BC concentration, AOD, Ångström exponent and effective radius are analyzed.

2. Observation Site and Instruments

The observation was conducted at the Semi–Arid Climate and Environment Observatory of Lanzhou University (SACOL, 35°57'N, 104°08'E, 1 965.8 m) (Huang et al., 2008) from November 2010 to February 2011. SACOL is about 48 km away from Lanzhou, which is situated on the southern bank of the Yellow River, in the Gansu

province of northwest China. SACOL is situated on a mountaintop called Cuiying, which is 1 965.8 m above sea level, in the Loess Plateau of China. The topography around SACOL consists of plains, ridges and mounds, with the elevation ranging between 1 714 and 2 089 m. The parent soil material is mainly quaternary aeolian loess, with the main soil type being sierozem. SACOL is covered with short grasses, such as stipa bungeana, artemisia frigida and leymus secalinus. The maximum surface temperature appears in July, and the minimum surface temperature appears in January. The maximum amount of precipitation falls in August. The instruments used in the paper include a depolarization lidar, a multi–angle absorption photometer and a sun photometer.

The depolarization lidar (L2S–SM II, NIES) uses a flash–lamp–pumped Nd:YAG laser as a light source. The output energy is approximately 20 mJ at both 532 nm and 1 064 nm, with a pulse repetition frequency of 10 Hz, a pulse width of approximately 10 ns and a beam diameter of 20 mm. The backscattered signal is received by a Schmidt Cassegrain telescope with the diameter of 20 cm and field of view of 1 mrad and then collimated and separated into wavelengths of 1 064 nm and 532 nm. The 1 064 nm wavelength is detected with an Avalanche PhotoDiode (APD), and the 532 nm wavelength is further separated into polarized parallel and perpendicular components. Then, each of these is detected via a Photo Multiplier Tube (PMT). The range resolution of the observational data is 6 m, and the temporal resolution is 15 min.

The BC mass concentration is observed via a multi–angle absorption photometer (MAAP5012, Thermo Electron). The sample flows through a downward tube and is deposited onto a glass fiber filter tape. In the detection chamber, the 670 nm light is transmitted into the forward hemisphere and then reflected into the back hemisphere, where it is measured by a series of photo–detectors, which are used to analyze the modification of the radiation fields. The upstream sample line is composed of a size–selective inlet ($PM_{2.5}$) and a downward tube (Tygon R–3603, 3 m long), and it is connected to the sample connector on the top panel of the MAAP5012. The last 1 m of the downward sample tube is optically shielded to prevent any light leakage into the detection chamber. The sample flow rate is 1 000 L/h, and the flow error is less than 1%. MAAP5012 uses a glass fiber filter (GF 10), the retention degree of which is 99.98%, and the filter is automatically changed when the light transmission reaches 20% or when the black carbon mass reaches 30 μg.

The mass of the BC is calculated using, $MBC=(1-\omega_0)\times X_1 \times A/\sigma_{BC}$, where *MBC* is the mass of the BC, ω_0 is the single scattering albedo, X_1 is the natural logarithm of the transmittance, *A* is the area of the particle–collecting spot (2.0 cm^2) and σ_{BC} is the scattering cross–section of the BC (6.6 m^2/g). Then, the BC concentration can be retrieved using, $CBC=\Delta MBC/Vol$, where ΔMBC is the variance of mass of the BC and *Vol* is the sample volume.

The sun photometer (CE–318, Cimel) measures the direct and scattering solar irradiance in the visible and near–infrared wavelengths of 1 020, 936, 870, 670, 440, 870p1, 870p2 and 870p3 nm. Its optical head has a sun collimator and a sky collimator, and the field–of–view of sun collimator and sky collimator both is 1.2°. The sun tracking is realized via the evaluation of the solar altitude with a four–quadrant detector. The sun photometer is now widely used in the atmospheric sciences to determine aerosol properties (i.e., AOD, Ångström exponent and precipitable water), such as in the validation of satellite remote sensing.

3. Cloud Discrimination of the Lidar Data

The cloud discrimination is based on the research of Mao et al. (2011), which was further developed by Cao et al. (2013). The key principle is that the lidar backscattering signal increases with height in the feature region between the cloud base and peak (BPR) and a trend function is defined in order to judge the variation trend of the lidar signal with height.

The trend function can be expressed as $f(R)=a+b-0.5c$, where *a* is the number of range bins whose range–corrected signal (RCS) is weaker than that of the central range bin in the first half of the window, *b* is the number of range bins whose RCS is stronger than that of the central range bin in the other half of the window and *c* is the number of range bins in the window. $f(R)>0$ indicates that the lidar signal increases with height. When $f(R)>0$, the window is enlarged, and $f(R)$ is recalculated until $f(R)=0$. The selected window is a candidate for BPR. The height with the maximum RCS is set as the peak; the initial range bin is the base. If $RCS_p/RCS_b>2$, the selected window is classified as the cloud layer, where the subscripts *p* and *b* stand for the cloud peak and base, respectively. The next step is over–detection rejection using $\Delta=P(R_p)-P(R_b)<\sigma$, where $P(R)$ is the lidar signal at range *R*, without the range square correction, and σ is the standard deviation of $P(R)$ in the range of 15–17 km. Finally, the adjustment of the cloud base height is performed. When $\sigma_1<2\sigma$, the cloud base height is reset as the height one range bin above the former cloud base height, where σ_1 is the standard deviation of $P(R)$ in the range from the cloud base to nine range bins above the cloud base.

4. Lidar Retrieval Algorithm

The algorithm is based on the research of Fernald (1984) and Klett (1981, 1985), which was intended to determine the aerosol extinction coefficient, backscattering coefficient and AOD.

The lidar equation is as follows:

$$P(z) = ECz^{-2}[\beta_1(z) + \beta_2(z)]T_1^2(z)T_2^2(z) \quad (1)$$

where, *z* is the range; $P(z)$ is the lidar backscattering signal after all the corrections, except the range square correction; *E* is the output laser pulse energy; *C* is the calibration constant, $\beta(z)$ is the backscattering coefficient, $T(z) = exp\left[-\int_0^z \sigma(z)\,dz\right]$ is the transmittance and $\sigma(z)$ is the extinction coefficient. The subscript 1 stands for aerosol, while the subscript *2* stands for atmospheric molecules. By inducing the extinction–to–backscatter ratio *S*, the solution of Equation (1) for aerosol backscattering is given by Equation (2).

$$\beta_1(z) = \frac{P(z)z^2 exp\left[-2(S_1 - S_2)\int_0^z \beta_2(z)dz\right]}{CE - 2S_1\int_0^z P(z)\,z^2\,exp\left[-2(S_1 - S_2)\int_0^z \beta_2(\dot{z})d\dot{z}\right]dz} - \beta_2(z) \quad (2)$$

where, β_2 is calculated via the Rayleigh scattering theory, using the US standard atmospheric profile, and $S_2=8\pi/3$. If the initial condition of the aerosol extinction coefficient at the reference height Z_c is available, Equation (2) leads to a numerical integration. In this paper, the backward solution is selected because it is more stable than the forward solution (Klett, 1981). The aerosol extinction coefficient is calculated as follows:

$$\sigma_1(z) = -\frac{S_1}{S_2}\sigma_2(z) + \frac{X(z)exp\left[2\left(\frac{S_1}{S_2} - 1\right)\int_z^{z_c}\sigma_2(\dot{z})d\dot{z}\right]}{\frac{X(z_c)}{\sigma_1(z_c) + \frac{S_1}{S_2}\sigma_2(z_c)} + 2\int_z^{z_c} X(\dot{z})\,exp\left[2\left(\frac{S_1}{S_2} - 1\right)\int_z^{z_c}\sigma_2(\ddot{z})\,d\ddot{z}\right]d\dot{z}} \quad (3)$$

where, $X(z)=P(z)z^2$ is the range–corrected signal, and S_1 is the aerosol extinction–to–backscatter ratio, or lidar ratio (LR). Then, the AOD can be calculated by integrating the aerosol extinction coefficient from the surface to the reference height.

In this algorithm, three parameters, the reference height, the aerosol extinction coefficient at the reference height and the LR, should be given first. When there were no clouds, the reference height was set at a height with a negligible particle load (Balis et al., 2006), or it was set as the cloud base height. The aerosol extinction coefficient at the reference height is equal to that of the atmospheric molecules.

LR is determined via the aerosols' size distribution, shape and composition (He et al., 2006). It varies temporally and spatially due to the inhomogeneous distribution of the aerosols (Ansmann et al., 1992), and this makes the retrieved aerosol extinction coefficient more relative than absolute (Larcheveque et al., 2002). Using the AOD product of AERONET (level 2.0) as a validation of LR calculation, the average LR of the BC was 63 sr, which is close to that used in the CALIPSO models, with a value of 70 sr for aerosol–type smoke (Omar et al., 2009) and between 50 sr to 70 sr for heavily polluted air (Ansmann et al., 2001).

5. Results

5.1. Variation of BC concentration

Figure 1 shows the wind rose during the observation from November 2010 to February 2011. The wind speed and wind direction were observed via boundary–layer meteorological measurements at the Semi–Arid Climate and Environment Observatory of Lanzhou University (SACOL), and the data were averaged every 30 minutes. The data indicate that southeast was the predominant wind direction during the observation at 18.8%. North was the second most often observed wind direction at 14.9%, followed by northwest wind at 12.5%. Overall, 91.8% of the time, the wind speed was less than 2.1 m/s; the average of wind speed was 1.2 m/s and the wind direction was 28°. The diurnal evolution of wind speed, wind direction and relative humidity can be seen in Figure 2. The wind speed was high during the nighttime, and its maximum, 2.9 m/s, occurred at 01:00 (local time). The minimum of wind speed, 2.1 m/s, occurred at 14:00. The wind direction showed an increasing trend toward variation. The relative humidity (RH) increased with time, reaching a maximum of 51.2% at 12:00, and then decreased to a minimum of 44.6% at 00:00.

Figure 3 shows the evolution of the daily average BC concentration as measured by MAAP5012 from November 2010 to February 2011, which was within the heating period. Overall, the daily average BC concentration was 2 334±1 546 ng/m^3 during the observation period. The BC concentration was higher in December 2010 (2 937±2 092 ng/m^3) than in November 2010 (2 369±1 365 ng/m^3), January 2011 (2 459±1 137 ng/m^3) or February 2011 (1 492±899 ng/m^3). SACOL locates at the southeast of Lanzhou city and northeast of a county town named Yuzhong. The surrounding environment of SACOL is rural area. The two major impact factors for pollutant levels are the emissions and dispersion. If the pollutant emission is constant, the dominant impact factors are the dispersion and transport of the pollutants. The average wind speed in November and December 2010 were almost the same, while the percentage of northwest wind in December 2010 was 3% larger than in November 2010, which means that much pollution was transported to SACOL from Lanzhou city and leaded to a larger value of BC concentration in December 2010 than in November 2010 (Table 1). In January and February 2011 the wind speeds were increased to 1.17 m/s and 1.56 m/s, leading to a much better dispersion. Especially in February 2011, the north wind prevailed (88.2%), resulting in less pollution to be transported to SACOL.

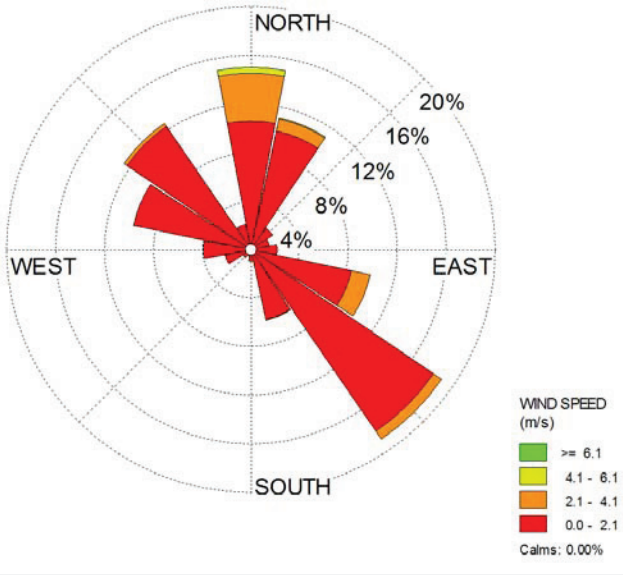

Figure 1. *Wind rose during the observation period from November 2010 to February 2011.*

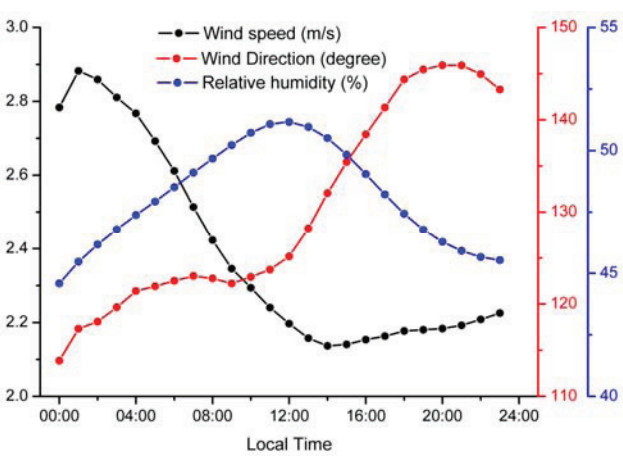

Figure 2. *Diurnal evolution of wind speed (black), wind direction (red) and relative humidity (blue) during the observation period from November 2010 to February 2011.*

Table 2 presents the statistics for BC mass concentrations during the observation period, such as the average, minimum, maximum, median and standard deviation. The minimum BC concentration was 121 ng/m^3, which occurred in December 2010, and the maximum was 20 380 ng/m^3, which occurred in February 2011. There were similar research projects at other stations. At Kanpur, in northern India, the BC concentration ranged from 6 000 to 20 000 ng/m^3 during December 2004 (Tripathi et al., 2005). In urban Tokyo, it decreased from 2 600 ng/m^3 to 500 ng/m^3 from 2003 to 2010 (Kondo et al., 2012). In remote areas, the BC concentration was rather small. For example, at Qilian Shan, in China, and in the Khumbu valley (5 079 m a.s.l.), BC values were 18 ng/m^3 to 72 ng/m^3 (Zhao et al., 2012) and 160 ng/m^3 (Marinoni et al., 2010), respectively.

Regarding the diurnal evolution of the average BC concentration (Figure 4), two maximums occurred at 10:00 and 20:00, with BC concentrations of 2 855 ng/m^3 and 2 623 ng/m^3, respectively, and two minimums occurred at 03:00 and 16:00, with BC concentrations of 2 185 ng/m^3 and 1 793 ng/m^3, respectively. The pollutant emissions and atmospheric dispersion are two important factors affecting the diurnal variation of BC concentrations. The

maximum at 10:00 was mainly caused by the enhancement of pollutant emissions from human activities, such as industry, vehicles and daily life, and the wind speed decreased after sunrise and reached a small value of 2.3 m/s. In the daytime, the wind speed mostly was below 2 m/s, and the inversion layer occurred after sunset, which was mainly responsible for the maximum at 20:00. In the afternoon, the planetary boundary layer develops well, with strong turbulence and convection. Thus, the atmospheric dispersion conditions were quite good in terms of diluting the pollutants, which was the reason for the minimum at 16:00. During the time period from 20:00 to 03:00 of the next day, human activities decreased substantially which caused to a low level of pollutant emissions, and the wind speed was high, leading to better dispersion conditions. This led to the minimum at 03:00.

The absorption coefficient of BC is the result of multiplying its mass concentration by the scattering cross–section (6.6 m^2/g). Figure 5 shows the diurnal evolution of BC's absorption coefficient during the observation, which indicates that the average value of the absorption coefficient was 0.015±0.009 1/km. Its minimum occurred at 16:00, with a value of 0.011 1/km, and its maximum occurred at 10:00, with a value of 0.018 1/km. As seen in Figures 4 and 5, the variation trend of the absorption coefficient was almost the same as that of BC mass concentration. The absorption coefficient is 6.6 times of mass concentration, so the reasons for the diurnal variation of BC absorption coefficient are the same with that for the diurnal change of BC mass concentrations that were presented above.

5.2. Vertical profile of the extinction coefficient and the evolution of AOD

The lidar data were cloud–screened first in order to remove the influence of the clouds. Then, the aerosol extinction coefficient and AOD were both determined at 532 nm. Figure 6 presents the vertical profiles of the aerosol extinction coefficient in November and December 2010, as well as in January and February 2011. The aerosols existed mostly between the surface of the Earth and 3 km in height, and the extinction coefficient decreased with height. The extinction coefficient was larger in January and February 2011 than in November and December 2010. Figure 7 shows the evolution of AOD from November 2010 to February 2011. The average AOD during the observation period was 0.26±0.2. Also, 0.2, 0.23, 0.32 and 0.31 were the average AOD values in November 2010, December 2010, January 2011 and February 2011, respectively. This indicated that the AODs in January and February 2011 were larger than those in November and December 2010, which agreed with the analysis of the extinction coefficient.

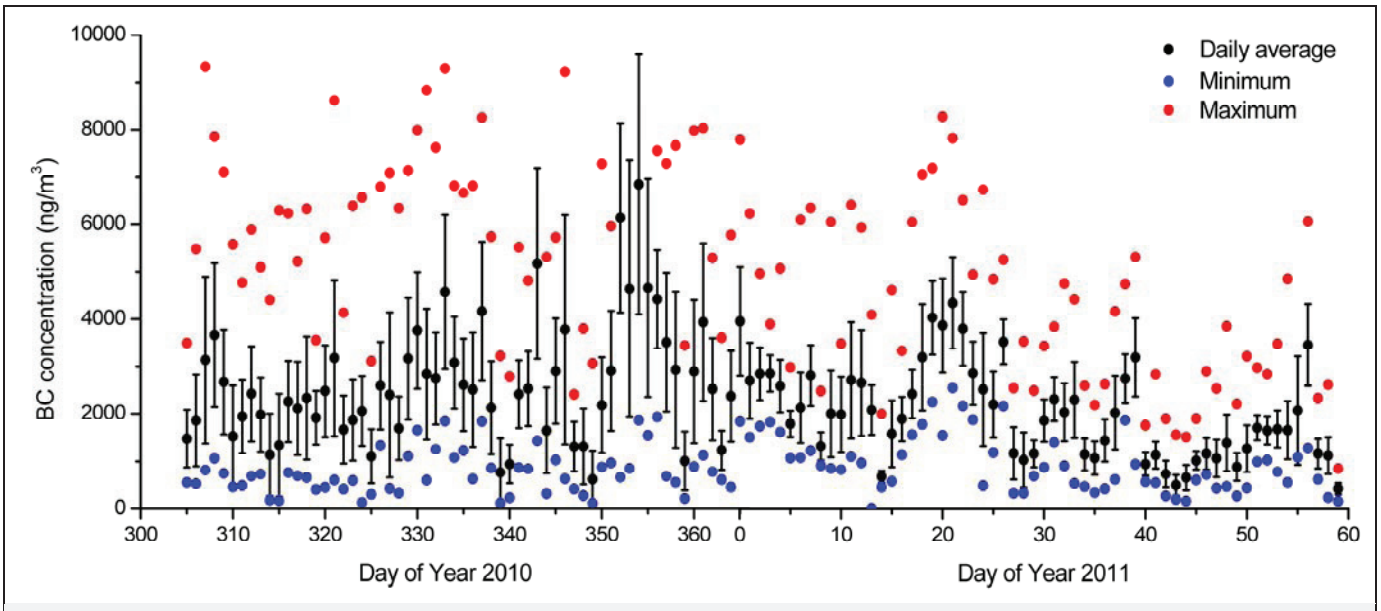

Figure 3. *Evolution of daily average BC concentration (black), daily minimum (blue) and maximum (red) of BC concentrations from November 2010 to February 2011.*

Table 1. *Statistics for monthly wind speed and wind direction during the observation*

Period	Average Wind Speed (m/s)	0–2.1 m/s	2.1–4.1	112.5–157.5	247.5–337.5
November 2010	0.99	97.2%	2.8%	42%	33%
December 2010	1.01	96.9%	3.1%	38%	38%
January 2011	1.17	94.3%	5.7%	43%	42%
February 2011	1.56	78.5%	19.3%	North wind 88.2%	

Table 2. *Statistics for BC mass concentrations (ng/m^3)*

Period	Average	Maximum	Minimum	Median	Standard Deviation
November 2010	2369	9326	136	2078	1365
December 2010	2937	12184	121	2400	2092
January 2011	2459	8281	336	2301	1137
February 2011	1492	20380	168	1280	899
All observation	2334	20380	121	1986	1546

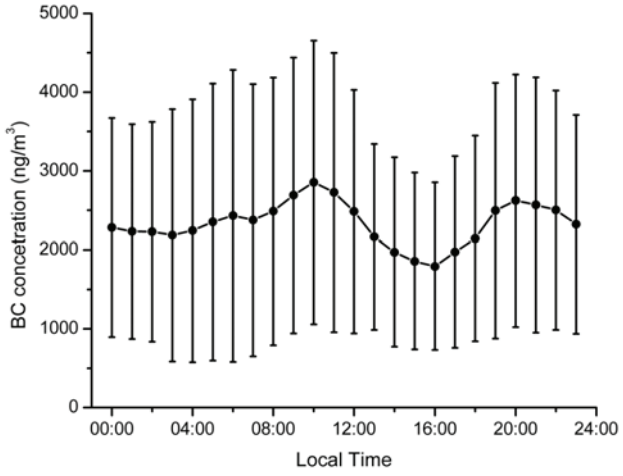

Figure 4. *Diurnal evolution of the average BC concentrations from November 2010 to February 2011.*

5.3. Vertical profile of depolarization ratio

The volume depolarization ratio used here, including atmospheric molecules and particulates, is defined as $\delta = P_{\perp} / P_{//}$, where $P_{\perp}$ and $P_{//}$ are the backscatter intensities in the planes of polarization perpendicular and parallel to the linearly polarized source (Noel et al., 2004). The depolarization ratio is a useful parameter for the study of aerosol microphysics because its deviation from zero indicates particle non–sphericity (Sakai et al., 2000).

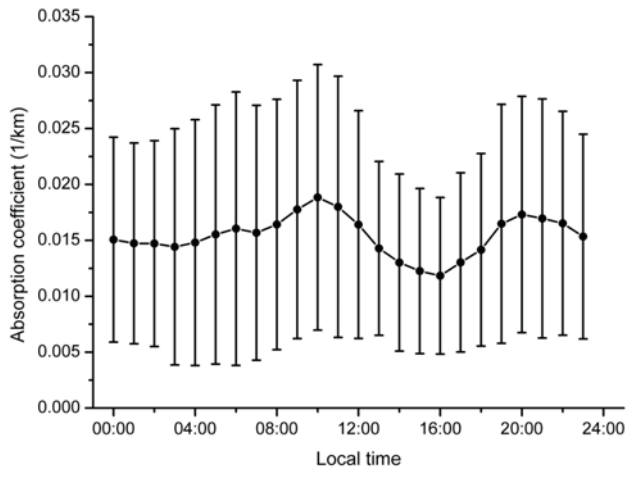

Figure 5. *Diurnal evolution of BC absorption coefficients from November 2010 to February 2011.*

Figure 8 shows the vertical distributions of the average volume depolarization ratio of black carbon aerosols in November and December 2010, as well as in January and February 2011. As in the above analysis, the aerosols existed mostly between Earth's surface and 3 km in height. Figure 8 only presents the volume depolarization ratio between Earth's surface and 3 km in height. In November and December 2010, the depolarization decreased from about 0.25 at the surface to nearly 0.125 at 2 km in height and then remained constant (black dots in Figure 8) or increased slightly with height (red dots in Figure 8), respectively. In January and February 2011, the vertical distributions of the depolarization ratio showed different vertical variations. From the surface of the Earth to about 1 km in height, the depolarization ratio was almost constant, with values of about 0.2 (blue dots in Figure 8) and 0.25 (green dots in Figure 8), respectively, and then increased with height. The average volume depolarization ratio during the observation period was 0.24. Also, 0.14, 0.17, 0.25 and 0.39 were the average volume depolarization ratios in November 2010, December 2010, January 2011 and February 2011, respectively.

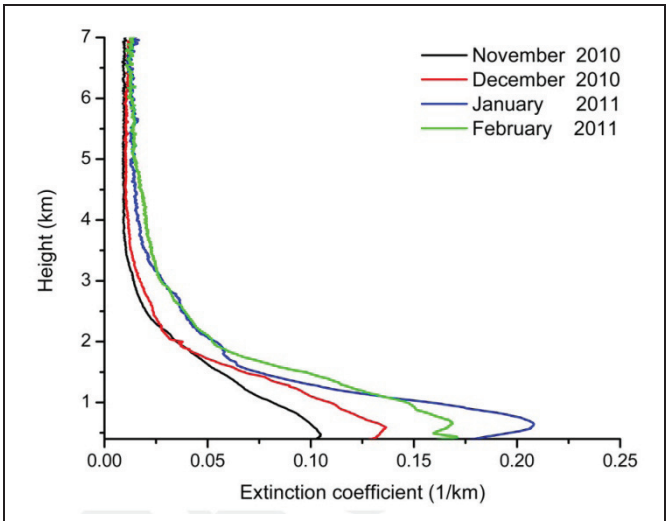

Figure 6. *Vertical profiles of the extinction coefficient in November and December 2010, as well as in January and February 2011.*

5.4. Evolutions of the Ångström exponent and effective radius

In this study, the level 2.0 products of AERONET (http://aeronet.gsfc.nasa.gov/) are used, including the Ångström exponent ($\alpha_{440/870\ nm}$) and effective radius. The Ångström exponent is defined as the wavelength's dependence on optical depth. Generally, the Ångström exponent ranges from 0.0 to 2.0, with smaller Ångström exponents corresponding to larger particles and vice–versa (Dubovik et al., 2002; Kim et al., 2004; Wang et al., 2013).

Figure 9a shows the frequency distribution of $\alpha_{440/870\ nm}$ for black carbon aerosols at SACOL from November 2010 to February 2011, which showed a normal distribution mode. The maximum frequency was about 27% within the range of 1.0 to 1.2. The average $\alpha_{440/870\ nm}$ during the observation period was 0.86±0.30. In addition, 0.90±0.34, 0.80±0.31 and 0.96±0.19 were the averages of $\alpha_{440/870\ nm}$ in November 2010, December 2010 and January 2011, respectively. In February 2011, there were only eight days of data, so the average was not calculated, while the data in February 2011 were included in the calculation of the average $\alpha_{440/870\ nm}$ during the observation period.

Figure 9b shows the frequency distribution of the effective radius of black carbon aerosols at SACOL from November 2010 to February 2011, which also showed a normal distribution mode. The maximum frequency was about 28% within the range of 0.4 μm to 0.5 μm. The average effective radius during the observation period was 0.54±0.17 μm. In addition, 0.48±0.13, 0.62±0.19 and 0.51±0.14 were the averages of the effective radius in November 2010, December 2010 and January 2011, respectively. In February 2011, there were only four days of data, so the average was not calculated, while the data in February 2011 were included in the calculation of the average of the effective radius during the observation.

Figure 10 shows the evolution of the daily average of $\alpha_{440/870\ nm}$ and the effective radius of black carbon aerosols during the observation period. Overall, their distributions were rather discrete. Generally, in November and December 2010, a certain proportion of $\alpha_{440/870\ nm}$ values were smaller than 0.6 (Figure 10a), which led to a smaller average than that seen in January 2011, as

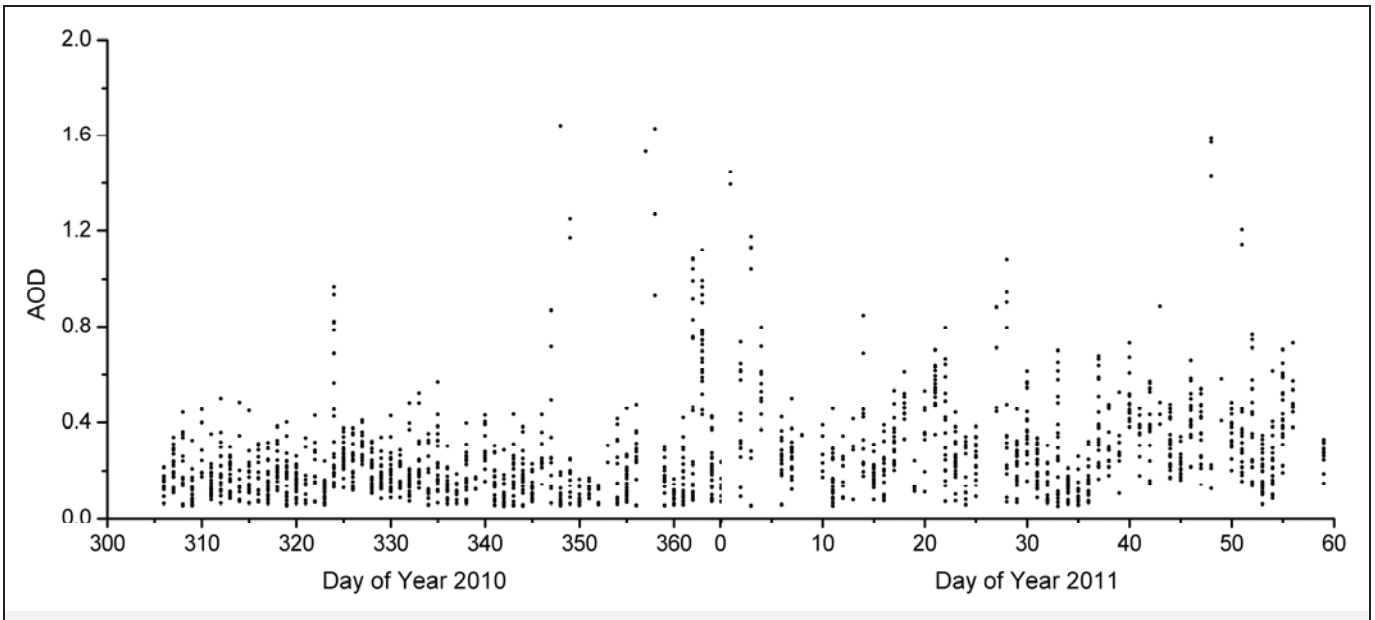

Figure 7. *Evolution of AOD, as retrieved from NIES lidar from November 2010 to February 2011.*

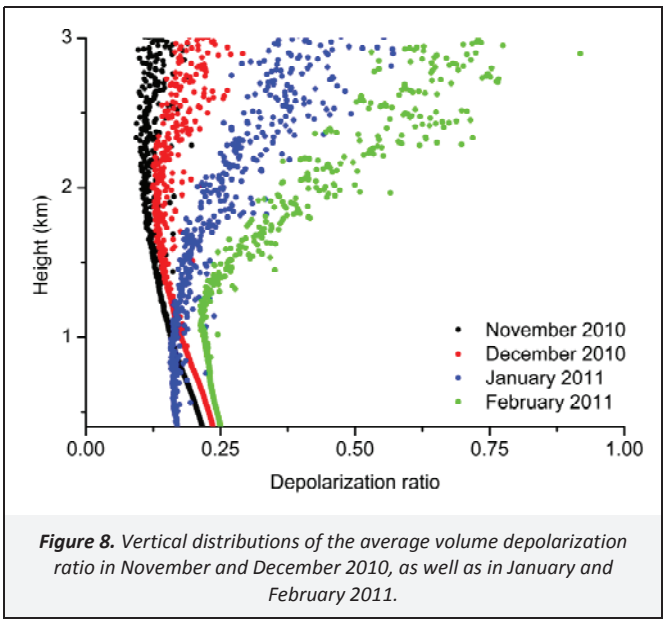

Figure 8. *Vertical distributions of the average volume depolarization ratio in November and December 2010, as well as in January and February 2011.*

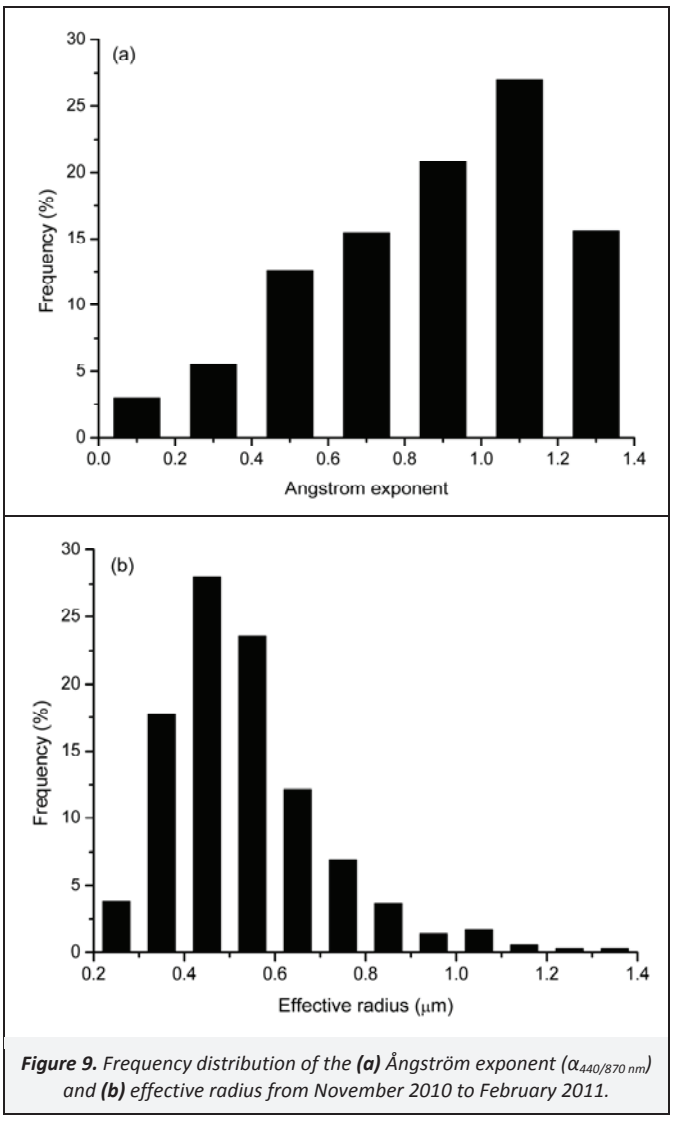

Figure 9. *Frequency distribution of the* ***(a)*** *Ångström exponent ($\alpha_{440/870\ nm}$) and* ***(b)*** *effective radius from November 2010 to February 2011.*

well as a larger effective radius, with values larger than 0.6 μm (Figure 10b). Comparing the evolutions of $\alpha_{440/870\ nm}$ and effective radius (Figure 11), they obviously present a negative correlation, showing that increasing $\alpha_{440/870\ nm}$ always accompanies decreasing effective radius.

6. Conclusions

The observations were carried out at the Semi–Arid Climate and Environment Observatory of Lanzhou University (SACOL) in the Loess Plateau of northwestern China, using a depolarization lidar, a multi–angle absorption photometer and a sun photometer. The time period from November 2010 to February 2011 was selected, which was during the heating period. It was believed that black carbon (BC) was the predominant type of aerosols. In this paper, the optical properties of BC, such as the depolarization ratio, extinction coefficient, optical depth, Ångström exponent and effective radius, were analyzed. The main results are as follows:

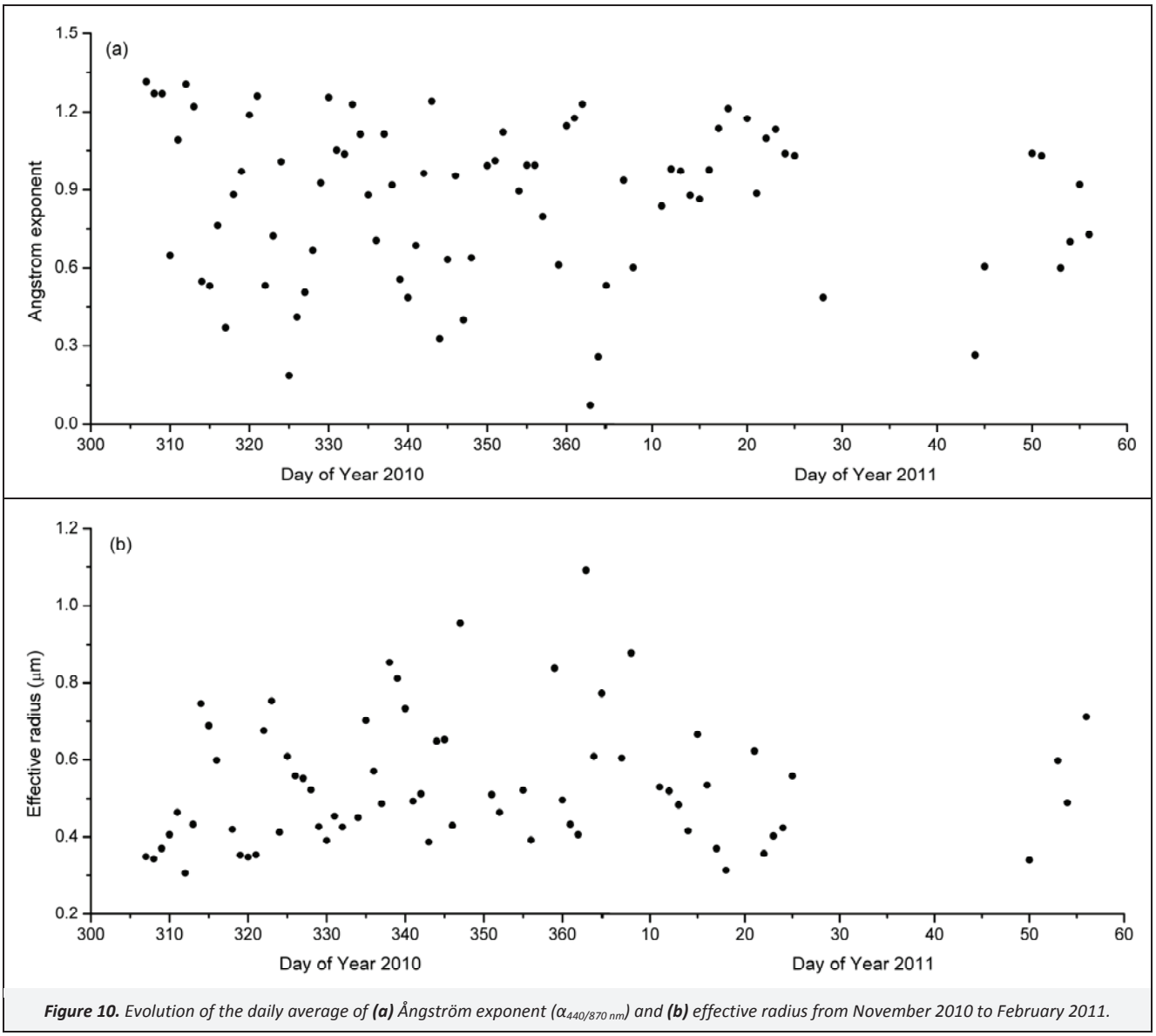

Figure 10. *Evolution of the daily average of* ***(a)*** *Ångström exponent ($\alpha_{440/870\ nm}$) and* ***(b)*** *effective radius from November 2010 to February 2011.*

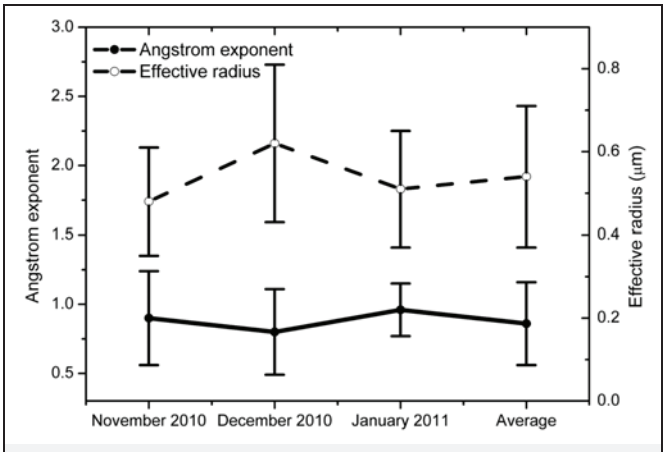

Figure 11. *Comparison between Ångström exponent ($\alpha_{440/870\ nm}$) and effective radius.*

(1) The average BC concentration was 2 334±1 546 ng/m^3 during the observation period. The diurnal evolution of BC concentration showed two maximums, which appeared at 10:00 and 20:00, and two minimums, which appeared at 03:00 and 16:00.

(2) The average AOD during the observation period was 0.26±0.2. The aerosols existed mostly between the surface of the Earth and a height of 3 km, and the extinction coefficient decreased with height.

(3) The average depolarization ratio, Ångström exponent $\alpha_{440/870\ nm}$ and effective radius of black carbon aerosols were 0.24, 0.86±0.30 and 0.54±0.17 μm, respectively.

(4) The maximum distribution frequency of $\alpha_{440/870\ nm}$ and the effective radius of black carbon aerosols were about 27% and 28% and had ranges of 1.0 to 1.2 and 0.4 μm to 0.5 μm, respectively.

Acknowledgments

The research is supported by the National Natural Science Foundation of China (41205112), the National Natural Science Foundation of China (41225018), the National Basic Research Program of China (2012CB955302) and the Program for Changjiang Scholars and Innovative Research Team in University (IRT1018). The authors are appreciated to all the reviewers for their valuable and critical comments without which this paper could not have proceeded to its present form. Thanks are given to the Semi–Arid Climate and Environment Observatory of Lanzhou University (SACOL) and the Aerosol Robotic Network (AERONET) staff for providing the corresponding data used in this study.

References

Ackerman, A.S., Toon, O.B., Stevens, D.E., Heymsfield, A.J., Ramanathan, V., Welton, E.J., 2000. Reduction of tropical cloudiness by soot. *Science* 288, 1042–1047.

Albrecht, B.A., 1989. Aerosols, cloud microphysics, and fractional cloudiness. *Science* 245, 1227–1230.

Ansmann, A., Wagner, F., Althausen, D., Muller, D., Herber, A., Wandinger, U., 2001. European pollution outbreaks during ACE 2: Lofted aerosol plumes observed with Raman lidar at the Portuguese coast. *Journal of Geophysical Research–Atmospheres* 106, 20725–20733.

Ansmann, A., Riebesell, M., Wandinger, U., Weitkamp, C., Voss, E., Lahmann, W., Michaelis, W., 1992. Combined raman elastic–backscatter LIDAR for vertical profiling of moisture, aerosol extinction, backscatter, and LIDAR ratio. *Applied Physics B–Photophysics and Laser Chemistry* 55, 18–28.

Atwater, M. A., 1970. Planetary albedo changes due to aerosols. *Science* 170, 64–66.

Babu, S.S., Moorthy, K.K., Satheesh, S.K., 2004. Aerosol black carbon over Arabian Sea during intermonsoon and summer monsoon seasons. *Geophysical Research Letters* 31, art. no. L06104.

Babu, S.S., Satheesh, S.K., Moorthy, K.K., 2002. Aerosol radiative forcing due to enhanced black carbon at an urban site in India. *Geophysical Research Letters* 29, art. no. 1880.

Balis, D., Amiridis, V., Kazadzis, S., Papayannis, A., Tsaknakis, G., Tzortzakis, S., Kalivitis, N., Vrekoussis, M., Kanakidou, M., Mihalopoulos, N., Chourdakis, G., Nickovic, S., Perez, C., Baldasano, J., Drakakis, M., 2006. Optical characteristics of desert dust over the east Mediterranean during summer: A case study. *Annales Geophysicae* 24, 807–821.

Bond, T.C., Streets, D.G., Yarber, K.F., Nelson, S.M., Woo, J.H., Klimont, Z., 2004. A technology–based global inventory of black and organic carbon emissions from combustion. *Journal of Geophysical Research–Atmospheres* 109, art. no. D14203.

Cao, X., Wang, Z., Tian, P., Wang, J., Zhang, L., Quan, X., 2013. Statistics of aerosol extinction coefficient profiles and optical depth using lidar measurement over Lanzhou, China since 2005–2008. *Journal of Quantitative Spectroscopy & Radiative Transfer* 122, 150–154.

Charlson, R. J., Pilat, M. J., 1969. Climate: the influence of aerosols. *Journal of Applied Meteorology* 8, 1001–1002.

Coakley, Jr. J. A., Cess, R. D., Yurevich, F. B., 1983. The effect of tropospheric aerosols on the earth's radiation budget: A parameterization for climate models. *Journal of Atmospheric Sciences* 40, 116–138.

Dubovik, O., Holben, B., Eck, T.F., Smirnov, A., Kaufman, Y.J., King, M.D., Tanre, D., Slutsker, I., 2002. Variability of absorption and optical properties of key aerosol types observed in worldwide locations. *Journal of the Atmospheric Sciences* 59, 590–608.

Fernald, F.G., 1984. Analysis of atmospheric lidar observations – some comments. *Applied Optics* 23, 652–653.

Grassl, H., 1975. Albedo reduction and radiative heating of clouds by absorbing aerosol particles. *Contributions to Atmospheric Physics* 48, 199–210.

Hansen, J., Sato, M., Ruedy, R., 1997. Radiative forcing and climate response. *Journal of Geophysical Research–Atmospheres* 102, 6831–6864.

He, Q.S., Li, C.C., Mao, J.T., Lau, A.K.H., Li, P.R., 2006. A study on the aerosol extinction–to–backscatter ratio with combination of micro–pulse lidar and MODIS over Hong Kong. *Atmospheric Chemistry and Physics* 6, 3243–3256.

Huang, J.P., Zhang, W., Zuo, J.Q., Bi, J.R., Shi, J.S., Wang, X., Chang, Z.L., Huang, Z.W., Yang, S., Zhang, B.D., Wang, G.Y., Feng, G.H., Yuan, J.Y., Zhang, L., Zuo, H.C., Wang, S.G., Fu, C.B., Chou, J.F., 2008. An overview of the semi–arid climate and environment research observatory over the Loess plateau. *Advances in Atmospheric Sciences* 25, 906–921.

Kim, D.H., Sohn, B.J., Nakajima, T., Takamura, T., Takemura, T., Choi, B.C., Yoon, S.C., 2004. Aerosol optical properties over east Asia determined from ground–based sky radiation measurements. *Journal of Geophysical Research–Atmospheres* 109, art. no. D02209.

Klett, J.D., 1985. Lidar inversion with variable backscatter extinction ratios. *Applied Optics* 24, 1638–1643.

Klett, J.D., 1981. Stable analytical inversion solution for processing lidar returns. *Applied Optics* 20, 211–220.

Kondo, Y., Ram, K., Takegawa, N., Sahu, L., Morino, Y., Liu, X., Ohara, T., 2012. Reduction of black carbon aerosols in Tokyo: Comparison of real–time observations with emission estimates. *Atmospheric Environment* 54, 242–249.

Koren, I., Kaufman, Y.J., Remer, L.A., Martins, J.V., 2004. Measurement of the effect of Amazon smoke on inhibition of cloud formation. *Science* 303, 1342–1345.

Larcheveque, G., Balin, I., Nessler, R., Quaglia, P., Simeonov, V., van den Bergh, H., Calpini, B., 2002. Development of a multiwavelength aerosol and water–vapor lidar at the Jungfraujoch Alpine Station (3580 m above sea level) in Switzerland. *Applied Optics* 41, 2781–2790.

Mao, F.Y., Gong, W., Zhu, Z.M., 2011. Simple multiscale algorithm for layer detection with lidar. *Applied Optics* 50, 6591–6598.

Marinoni, A., Cristofanelli, P., Laj, P., Duchi, R., Calzolari, F., Decesari, S., Sellegri, K., Vuillermoz, E., Verza, G.P., Villani, P., Bonasoni, P., 2010. Aerosol mass and black carbon concentrations, a two year record at NCO–P (5079 m, Southern Himalayas). *Atmospheric Chemistry and Physics* 10, 8551–8562.

McCormick, R. A., Ludwig, J. H., 1967. Climate modification by atmospheric aerosols. *Science* 156, 1358–1359.

Noel, V., Winker, D.M., McGill, M., Lawson, P., 2004. Classification of particle shapes from lidar depolarization ratio in convective ice clouds compared to in situ observations during crystal–face. *Journal of Geophysical Research–Atmospheres* 109, art. no. D24213.

Omar, A.H., Winker, D.M., Kittaka, C., Vaughan, M.A., Liu, Z.Y., Hu, Y.X., Trepte, C.R., Rogers, R.R., Ferrare, R.A., Lee, K.P., Kuehn, R.E., Hostetler, C.A., 2009. The CALIPSO automated aerosol classification and lidar ratio selection algorithm. *Journal of Atmospheric and Oceanic Technology* 26, 1994–2014.

Ramanathan, V., Carmichael, G., 2008. Global and regional climate changes due to black carbon. *Nature Geoscience* 1, 221–227.

Sakai, T., Shibata, T., Kwon, S.A., Kim, Y.S., Tamura, K., Iwasaka, Y., 2000. Free tropospheric aerosol backscatter, depolarization ratio, and relative humidity measured with the Raman lidar at Nagoya in 1994–1997: Contributions of aerosols from the Asian continent and the Pacific Ocean. *Atmospheric Environment* 34, 431–442.

Sasano, Y., 1996. Tropospheric aerosol extinction coefficient profiles derived from scanning lidar measurements over Tsukuba, Japan, from 1990 to 1993. *Applied Optics* 35, 4941–4952.

Schwarz, J.P., Gao, R.S., Fahey, D.W., Thomson, D.S., Watts, L.A., Wilson, J.C., Reeves, J.M., Darbeheshti, M., Baumgardner, D.G., Kok, G.L., Chung, S.H., Schulz, M., Hendricks, J., Lauer, A., Karcher, B., Slowik, J.G., Rosenlof, K.H., Thompson, T.L., Langford, A.O., Loewenstein, M., Aikin, K.C., 2006. Single–particle measurements of midlatitude black carbon and light–scattering aerosols from the boundary layer to the lower stratosphere. *Journal of Geophysical Research–Atmospheres* 111, art. no. D16207.

Shi, G. Y., Wang, B., Zhang, H., Zhao, J. Q., Tan, S. C., Wen, T. X., 2008. The radiative and climatic effects of atmospheric aerosols. *Chinese Journal of Atmospheric Sciences* 32, 826–840 (in Chinese).

Srivastava, A.K., Ram, K., Pant, P., Hegde, P., Joshi, H., 2012. Black carbon aerosols over Manora peak in the Indian Himalayan foothills: Implications for climate forcing. *Environmental Research Letters* 7, art. no. 014002.

Tripathi, S.N., Dey, S., Tare, V., Satheesh, S.K., 2005. Aerosol black carbon radiative forcing at an industrial city in Northern India. *Geophysical Research Letters* 32, art. no. 08802.

Twomey, S., 1977. The influence of pollution on the shortwave albedo of clouds. *Journal of the Atmospheric Sciences* 34, 1149–1152.

Wang, H.B., Zhang, L., Cao, X.J., Zhang, Z.W., Liang, J.N., 2013. A–train satellite measurements of dust aerosol distributions over Northern China. *Journal of Quantitative Spectroscopy & Radiative Transfer* 122, 170–179.

Zhao, S.Y., Ming, J., Xiao, C.D., Sun, W.J., Qin, X., 2012. A preliminary study on measurements of black carbon in the atmosphere of Northwest Qilian Shan. *Journal of Environmental Sciences–China* 24, 152–159.